Noncontact RF Vital Sign Sensor for Continuous Monitoring of Driver Status

Jin-Kwan Park, *Student Member, IEEE*, Yunseog Hong, Hyunjae Lee, *Student Member, IEEE*, Chorom Jang, *Student Member, IEEE*, Gi-Ho Yun, Hee-Jo Lee, and Jong-Gwan Yook, *Senior Member, IEEE*

***Abstract*—In this paper, a radio frequency vital sign sensor based on double voltage-controlled oscillators (VCOs) combined with a switchable phase-locked loop (PLL) is proposed for a noncontact remote vital sign sensing system. Our sensing system primarily detects the periodic movements of the human lungs and the hearts via the impedance variation of the resonator. With a change in impedance, both the VCO oscillation frequency and the PLL feedback voltage also change. Thus, by tracking the feedback voltage of the PLL, breath and heart rate signals can be acquired simultaneously. However, as the distance between the body and the sensor varies, there are certain points with minimal sensitivity, making it is quite difficult to detect vital signs. These points, called impedance null points, periodically occur at distances proportional to the wavelength. To overcome the impedance null point problem, two resonators operating at different frequencies, 2.40 and 2.76 GHz, are employed as receiving components. In an experiment to investigate the sensing performance as a function of distance, the measurement distance was accurately controlled by a linear actuator. Furthermore, to evaluate the sensing performance in a real environment, experiments were carried out with a male and a female subject in a static vehicle. To demonstrate the real-time vital sign monitoring capability, spectrograms were utilized, and the accuracy was assessed relative to reference sensors. Based on the results, it is demonstrated that the proposed remote sensor can reliably detect vital signs in a real vehicle environment.**

***Index Terms*—Continuous monitoring, driver diagnosis, impedance null points, noncontact detection, RF proximity vital sign sensor, switching circuit.**

Manuscript received September 28, 2018; revised January 29, 2019 and March 18, 2019; accepted March 23, 2019. Date of publication March 29, 2019; date of current version May 24, 2019. This work was supported in part by MSIT (Ministry of Science and ICT), Korea, under the ITRC (Information Technology Research Center) support program (IITP-2017-2013-0-00680) supervised by IITP (Institute for Information & Communications Technology Promotion), and in part by the National Research Foundation of Korea (NRF) grant funded by the Korea government (MSIT) (NRF-2017R1A2B2011724). This paper was recommended by Associate Editor H. Yu. *(Corresponding author: Jong-Gwan Yook.)*

J.-K Park, H. Lee, C. Jang, and J.-G. Yook are with the Department of Electrical and Electronic Engineering, Yonsei University, Seoul 03722, South Korea (e-mail: paladin91@yonsei.ac.kr; dblovewls@yonsei.ac.kr; chorom@yonsei.ac.kr; jgyook@yonsei.ac.kr).

Y. Hong is with the AESA Radar R&D Center, Hanwha Systems, Gyeonggi-Do 17121, South Korea (e-mail: yunseok.hong@hanwha.com).

G.-H. Yun is with the Department of Information and Communication Engineering, Sungkyul University, Gyeonggi-Do 14097, South Korea (e-mail: ghyun@sungkyul.ac.kr).

H.-J. Lee is with the Department of Physics Education, College of Eduction, Daegu University, Daegu 38453, South Korea (e-mail: hjlee@daegu.ac.kr).

Color versions of one or more of the figures in this paper are available online at http://ieeexplore.ieee.org.

Digital Object Identifier 10.1109/TBCAS.2019.2908198

I. Introduction

In recent years, continuous monitoring of human physiological states and human health has received considerable attention due to ever-increasing safety and healthcare concerns, such as monitoring body temperature [1], intracranial pressure [2], blood pressure [3], blood uric acid [4]–[6], blood glucose [7], [8], blood ketone [9], [10], and stress [11]. Moreover, methods of tracking driver status to estimate drowsiness have been developed and studied.

Continuous driver condition monitoring is particularly important because approximately 20% of fatal car crashes are caused by driver drowsiness [12]. Due to the high risk posed by drowsiness, several techniques for recognizing driver drowsiness have been studied, such as monitoring the movement of the vehicle, changes in facial images and changes in physiological signals. Drowsiness can be estimated from vehicle movements by considering the lane position during travel, the position of the steering wheel, the yaw angle of the vehicle and the traveling speed of the vehicle [13], [14]. However, this method has limitations because it can identify the risk only after a potentially dangerous situation has occurred, making it difficult to prevent accidents. Changes in facial images can be utilized to predict drowsiness based on the blink rate of the eyes [15], [16] and the movement of the head [17]. However, the accuracy of a camera-based method is affected by the angle of the camera and various lighting conditions. Additionally, such a method requires a high-performance system to store the images and perform imaging processing. Estimating drowsiness based on physiological signals is also possible by monitoring vital signs, such as breath rate [18] and heart rate [19]. By measuring these vital signs in real time, decisions can be made without being affected by environmental conditions and before a fatal accident occurs. Thus, various continuous vital sign monitoring methods are under development to prevent accidents caused by drowsy driving.

For the continuous monitoring of vital signs, the used sensors should be appropriate for long-term monitoring and require a fast response time, good repeatability and robustness to the environment. To satisfy these requirements, various sensing mechanisms have been studied. One example is a piezoelectric sensor [20], [21], which transforms the mechanical pressure caused by arterial pulsations into electrical signals. However, such a sensor must be tightly fastened to the subject and is vulnerable to frictional electricity. Therefore, piezoelectric sensors are not optimal for continuous monitoring. Another approach involves a photoplethysmography (PPG) sensor [22], [23], which measures reflected or transmitted light modulated by the periodicity of the heartbeat and respiration. However, such a sensor must also be very closely attached to the skin, and external light must be blocked to enable precise vital sign measurements. Thus, such sensors are also difficult to employ for monitoring the vital signs of a driver. The third method is to use radio frequency (RF)-based sensors, which can be divided into Doppler radar sensors and proximity impedance sensors. A single-tone continuous-wave (CW) Doppler-radar-based sensor [24]–[26] measures the changes in phase induced by the Doppler shift. The detection range of Doppler radar is very long, but this is a double-edged sword because it leads to measurement difficulties when multiple subjects are in range of the radar system. Since CW Doppler-radar-based sensors do not transmit an instantaneous bandwidth, there is no range resolution available to distinguish vital signs from multiple subjects. As an alternative, frequency-modulated continuous-wave (FMCW) Doppler-radar-based sensors [27], [28] show potential to solve the multiple-subject problem for vital sign monitoring. FMCW Doppler-radar-based sensors transmit signals with frequency-modulated periodic waveform changes over time. By using the frequency difference between the transmitter and receiver, the position of the target can be localized. Moreover, by using the phase deviation, vital signs detected from different positions can be distinguished. However, these sensors have high noise figures and low isolation between the transmitter and receiver for the extraction of accurate results. Therefore, this method suffers from problems of system complexity and cost. For these reasons, further investigations of these sensors are necessary to improve their convenience of use, freedom from cointerference, and fabrication costs. On the other hand, RF proximity impedance sensors have been developed for biomedical applications due to their suitability for use in noncontact, nondestructive and noninvasive measurements [29]–[32]. In addition, when combined with an active circuit, these sensors can be used in commercial mobile communication systems. Note that various vital sign sensors based on RF proximity-sensing impedance systems have been proposed, e.g., a surface acoustic wave (SAW) filter system [33], a phase-locked loop (PLL) system [34], and an interferometric system [35]. However, these sensors have short detection ranges due to their impedance null characteristics. Specifically, periodic null points occur where the incident and reflected waves cancel each other out. In these regions, the impedance of the receiver drastically changes with slight variations in the measurement position, which leads to erroneous results.

In this paper, an RF vital sign sensor based on a switchable circuit is proposed, and it is shown to be appropriate for the continuous monitoring of driver status. This sensor has several advantages. First, it has no need to be tightly fastened to the subject, thus facilitating continuous vital sign monitoring. With noncontact vital sign measurements, drivers are not inconvenienced by any restraints and do not need to equip a device every time vital signs are to be measured. Second, the detection range of the proposed sensor has been extended to enable its use in a vehicle environment. In our previous work, the investigated RF impedance-based sensors had a limited detection range due to the null point problem and encountered difficulties when applied in real-world environments. By comparison, the detection range of the proposed sensor is increased by a factor of eight by switching between two circuits operating at different frequencies to avoid impedance null points. Third, excellent sensor performance without an increase in the fabrication cost. By means of resonator miniaturization and selective combination with the active circuit, the sensor size is kept the same, and the sensor cost is reduced through sharing of the feedback circuits. Moreover, the performance of the proposed sensor shows no degradation with the increase in its detection range. It is demonstrated that a driver's condition can be continuously monitored by measuring his or her vital signs (hear rate and breath rate) via this noncontact RF method.

II. Sensor Design

A. Principle

The principle of the proposed vital sign sensing transducer is based on resonator impedance variations caused by human respiration and heartbeat. As a subject breathes and his or her heart beats, the volumes of the lungs and heart periodically vary. These periodic movements cause impedance variations in a resonator as a function of distance, giving rise to detect vital sign signals.

The impedance of a resonator is a function of the distance between the resonator and the subject:

$$Z_r = \eta_0 \frac{\eta_1 + j\eta_0 tan\beta d}{\eta_0 + j\eta_1 tan\beta d}, \quad (1)$$

where Z_r, η_0, η_1, β, and d are the input impedance of the resonator, the intrinsic impedance of air, the intrinsic impedance of the material, the propagation constant of the electromagnetic waves in air, and the distance between the resonator and the subject, respectively. Based on Eq. (1), the relation between the impedance and the wavenumber can be derived by normalizing the distance with respect to the operating frequency. For $Z_r = R_r + jX_r$, the resistance (R_r) and reactance (X_r) versus distance are presented in Fig. 1(a) and Fig. 1(b), respectively. Since the proposed sensor detects the periodic mechanical displacements of the heart and lungs, changes in the impedance with respect to distance are significant for sensing performance. Furthermore, since the proposed sensor is based on voltage-controlled oscillators (VCOs) combined with a PLL, the reactance plays a significant role. Therefore, the first derivative of the reactance is derived, as shown in Fig. 2(a). To clearly identify the effect of the distance on the first derivative of the reactance, the second derivative of the reactance is also derived, as shown in Fig. 2(b). Except near the null points, the second derivative of the reactance exhibits a flat slope. However, near a null point, the second derivative of the reactance fluctuates dramatically. Such a point occurs at every half-wavelength of the device and degrades the performance of the sensor, giving it a limited detection range.

However, since the wavelength is a function of the frequency, devices operating at different frequencies have different null

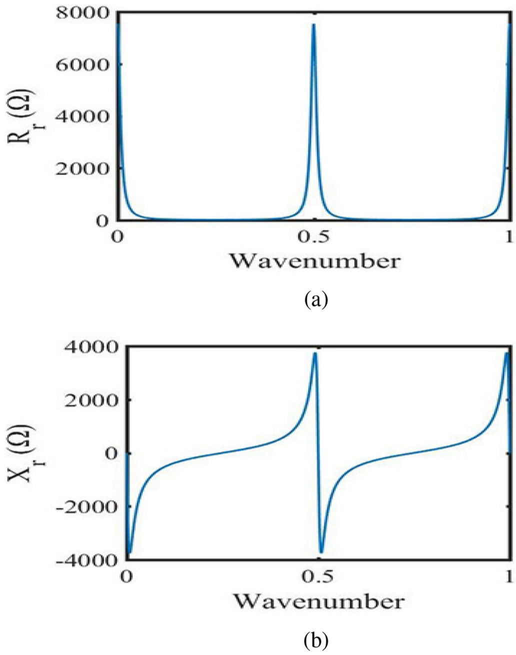

Fig. 1. Impedance versus wavenumber. (a) Resistance. (b) Reactance.

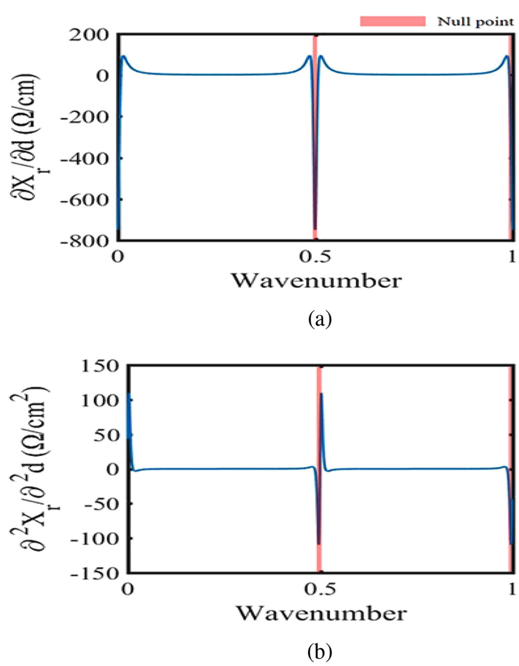

Fig. 2. Impedance null principle versus wavenumber. (a) First derivative impedance variation of the reactance. (b) Second derivative impedance variation of the reactance.

points, as shown in Fig. 3. Two resonators operating at different frequencies are used: 2.76 GHz (resonator 1) and 2.4 GHz (resonator 2). The operating frequency of 2.4 GHz is selected because it is in the industrial-scientific-medical (ISM) band, which is a specific frequency band for wireless sensing platforms. In addition, 2.76 GHz is selected because, as shown in Table I, the $N_{counter}$ values of 2.4 GHz and 2.76 GHz (20 and 23, respectively) are relatively prime. Therefore, by selecting

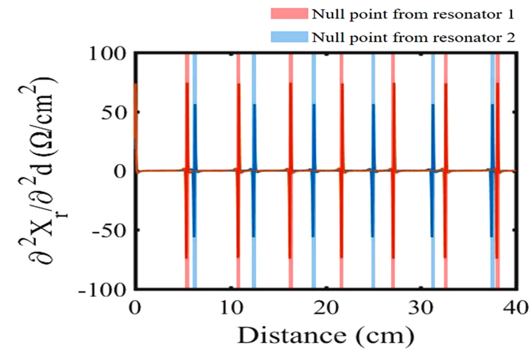

Fig. 3. Impedance null points of two independent resonators.

TABLE I
LOCK FREQUENCY PARAMETERS

Lock Frequency	Reference Frequency	Division Ratio	Prescaler Value	$N_{counter}$	$N_{counter}-1$ (bit)						Modulus (bit)	
					N_5	N_4	N_3	N_2	N_1	N_0	S_1	S_0
2.4 GHz	30 MHz	80	4	20	0	1	0	0	1	1	0	0
2.76 GHz		92		23	0	1	0	1	1	0	0	0

these frequencies, regions in which the null points overlap can be avoided, thus maximizing the detection range. Although multiple null points occur periodically as the distance increases to 40 cm, the null points of the two resonators do not overlap. By exploiting this characteristic, the null point problem can be effectively avoided without increasing the complexity of the circuit.

B. Configuration of the System

Fig. 4(a) shows the proposed dual-mode planar-type shorting-pin resonators. By adding multiple shorting pins to each resonator, the radiation gain can be increased while reducing the resonator size [36]. The upper resonator (resonator 1) operates in the higher-frequency region (3.08 GHz), while the lower resonator (resonator 2) operates in the lower-frequency region (2.625 GHz), as shown in Fig. 4(b). Moreover, the loaded quality factors (Q_L) of the resonators, which are related to their output signal levels, are 36.67 and 35.47, respectively. The relation between Q_L and the output signal level is shown as follows:

$$\Delta\omega = -\frac{\omega_0 \Delta\phi}{2Q_L}, \tag{2}$$

where $\Delta\omega$ is the frequency deviation, ω_0 is the resonant frequency, and $\Delta\phi$ is the phase variation. As shown by Eq. (2), a low Q_L of the resonator induces large frequency deviations in response to the phase variations caused by the mechanical displacements of the heart and lungs. Therefore, in our proposed sensor, a low Q_L value is desirable to achieve a high output signal. The difference between the measured and simulated results is caused by the additional length introduced by the components of the physical system, including the connectors and the microstrip line. Fig. 4(c) shows the isolation characteristics between the two resonators, demonstrating that the interaction between the two resonators is negligible. Thus, by adding

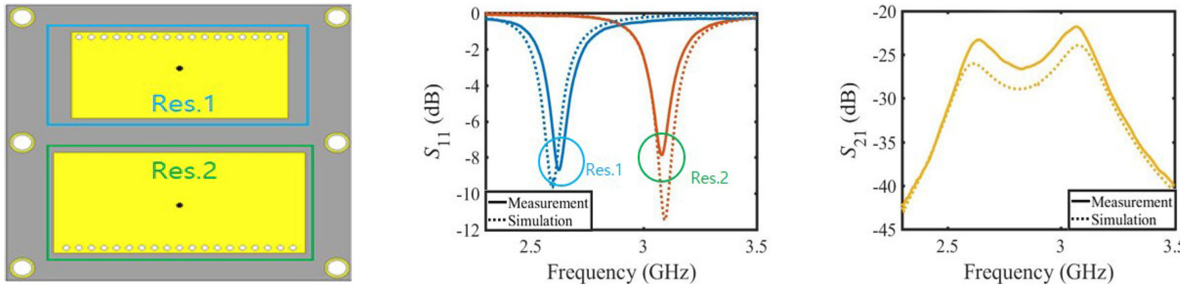

(a) (b) (c)

Fig. 4. Characteristics of the resonators. (a) Schematic of the proposed resonators. (b) Radiation properties of the resonators. (c) Isolation properties of the resonators.

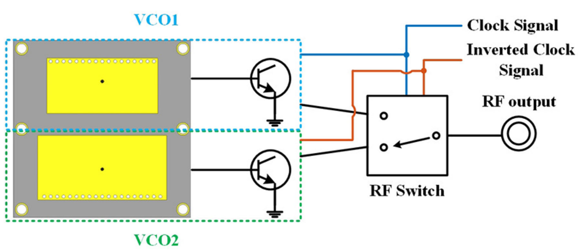

Fig. 5. VCO switching circuit.

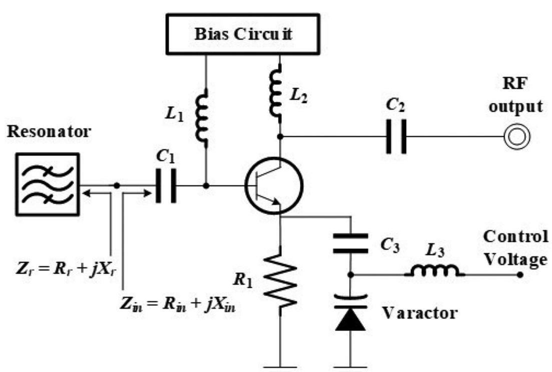

Fig. 6. Circuit diagram for each VCO.

multiple shorting pins to the resonators, it becomes possible to place both resonators in the same plane without any interactions.

For the selective detection of vital signs, each resonator is associated with a VCO circuit and connected to an RF switch, as shown in Fig. 5. The RF switch passes the signals from VCO1 and VCO2 to the next stage of the sensor, according to the input clock signal. The circuit diagram for each VCO is presented in Fig. 6; a series feedback method is adopted, and the resonator is connected to the base terminal of a bipolar junction transistor (BJT). The VCO is designed on the basis of the negative resistance method, as follows:

$$\begin{aligned} R_r + R_{in} &< 0, \\ X_r + X_{in} &= 0, \end{aligned} \tag{3}$$

where $Z_{in} = R_{in} + jX_{in}$ is the input impedance of the circuit looking into the base terminal of the BJT and $Z_r = R_r + jX_r$ is the input impedance of the resonator.

Because a BJT is used, R_{in} can be negative. In addition, by using a hyperabrupt junction tuning varactor diode, an inductor (L_3), and two capacitors (C_1 and C_3), X_{in} can be adjusted as follows:

$$X_{in} = \left\{ \left(j\omega_0 L_3 || \frac{1}{j\omega_0 C_v} \right) + \frac{1}{j\omega_0 C_3} \right\} || \frac{1}{j\omega_0 C_1}. \tag{4}$$

The varactor diode has a variable capacitance (C_v) that varies with the change in the feedback voltage from 7.37 pF (0 V) to 2.09 pF (5 V), and this characteristic causes the oscillation frequency to be directly proportional to the feedback voltage. Since the imaginary condition is more difficult to meet, the reactance determines the oscillation frequency.

The measured average gains of the fabricated VCO1 and VCO2 are 19 MHz/V and 11.2 MHz/V, respectively, and they have respective oscillation frequency ranges of 95 MHz and 56 MHz. The bias circuit is composed of a voltage divider to reduce the DC power supply, and the current consumption of the BJT is 10.8 mA at a collector-emitter voltage of 4 V. The capacitors (C_1, C_2 and C_3) are used to block the DC voltage from entering the RF signal path, and the inductors (L_1 and L_2) are used to prevent the RF signal from being induced into the DC bias path.

Fig. 7(a) shows the operating principle of the proposed switchable PLL system, and the general feedback PLL system is shown in Fig. 7(b). The operating principle of the general feedback PLL system for vital sign measurement is as follows [34]: When the RF signal from a VCO reaches the PLL, the PLL compares the frequency between the incoming signal and the lock frequency. Note that the lock frequency is determined by multiplying the reference frequency by a frequency division ratio. The reference frequency is injected from a stable oscillator such as a crystal oscillator or signal generator, and the frequency division ratio can be modified by the user. When the lock frequency is lower than the incoming signal frequency, the output voltage of the loop filter decreases to lower the oscillation frequency of the VCO. By contrast, if the lock frequency exceeds the incoming signal frequency, the output voltage of the loop filter increases. This feedback loop causes the VCO frequency to become equal to the lock frequency such that the

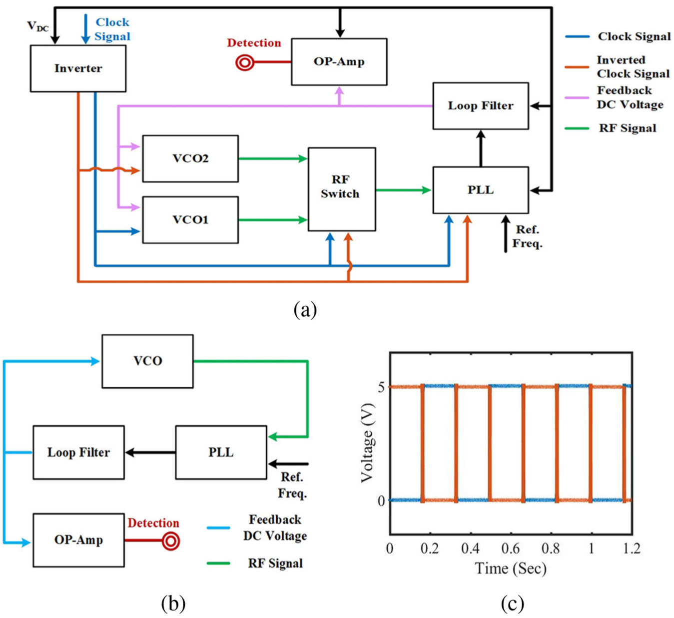

Fig. 7. Operating principle of the system. (a) Proposed system. (b) General feedback PLL system. (c) Measured results for the clock signal and inverted clock signal.

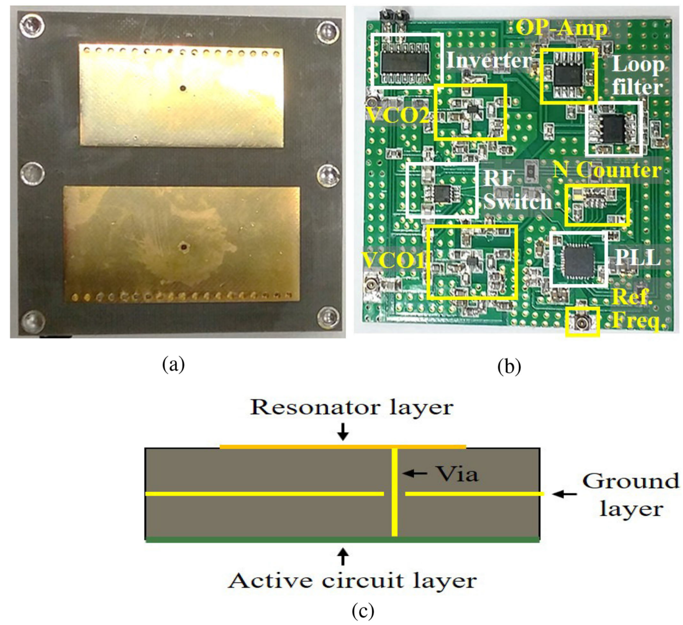

Fig. 8. Fabricated sensor. (a) Top view of the proposed sensor (planar resonators). (b) Bottom view of the proposed sensor (active circuit). (c) Side view of the proposed sensor.

system produces a stable frequency. Thus, when the volume of the lungs or heart changes, the X_r of the resonator causes the oscillation frequency of the VCO to change. Then, the PLL adjusts the feedback voltage to make the output frequency equal to the lock frequency. Consequently, as the volume of the lungs or heart periodically varies, the feedback voltage follows the target vital sign. However, a general feedback PLL sensor has a limited detection range, i.e., up to the first null point.

In contrast to this general circuit, the components of the proposed system are controlled by a clock signal. The operation of the VCOs, the traversal path of the RF switch, and the lock frequency of the PLL are all controlled by the clock signal, as shown in Fig. 7(c). The frequency of the clock signal is 3 Hz, and the waveform of this signal is a periodic square function with an amplitude of 5 V. Additionally, an inverted clock signal is applied by means of an inverter to prevent clock nonsynchronization. By using a programmable PLL, the lock frequency can be controlled by a binary bit signal, as shown in Table I. The frequency division ratio is programmed via the multiplication of a prescaler value and $N_{counter}$, and the value of $N_{counter} - 1$ is supplied by an external input to the PLL. By supplying the clock signal and the inverted clock signal to N_0 and N_2, the lock frequency can be easily set to either 2.4 GHz or 2.76 GHz. Thus, by means of this switchable system, the sensor can be operated at multiple frequencies, thus extending its range without increasing the complexity, size, or cost of the circuit.

C. Fabrication of the Sensor and Experimental Setup

The proposed sensor has been fabricated on a printed circuit board (PCB) of 30 mil in thickness with a dielectric constant (ϵ_r) of 2.2 and a loss tangent ($\tan\delta$) of 0.0009. The sensor is composed of three layers: the resonator layer, the active circuit layer and the ground layer. Each resonator is vertically interconnected to the active circuit through via holes, and they share a common ground plane in the middle layer to reduce the volume of the sensor, as shown in Fig. 8(c). Fig. 8(a) shows the fabricated planar-type shorting-pin resonators. In overall board size, the resonators occupy an area of 55 mm $\times$ 55 mm. The upper resonator has dimensions of 34.4 mm $\times$ 17.2 mm, and the lower resonator has dimensions of 40 mm $\times$ 20 mm. Fig. 8(b) shows the active circuit system part of the proposed sensor. VCO1 and VCO2, which are connected to the resonators, are each constructed using a BJT (BFP420) and a varactor diode (SMV1245). The output of each VCO is routed to a single-pole double-throw (SPDT) RF switch (HMC284), and the output of the RF switch is sent to the PLL IC (HMC698LP5). The PLL IC has a built-in phase-frequency detector (PFD), and the output signal of the PFD is sent to a loop filter (OP27). The reference signal, with a frequency of 30 MHz, is generated by a crystal oscillator (FH3000007) and injected through a coaxial microjack. The feedback voltage from the loop filter is supplied to the varactor diode of each VCO and, at the same time, is amplified by an operational amplifier (LM2904) for data acquisition. The clock signal is generated using a function generator (33510B) and inverted by an inverter (74HCT04D) to switch the circuit.

Two types of experiments were conducted. First, to identify the impedance null points and characterize the sensing ability of the proposed sensor, an experiment was carried out as shown in Fig. 9. The measurements were conducted using a vector network analyzer (E6071B), and the distance (d) was adjusted by means of a linear actuator. The resonator was fixed on the linear actuator using a 3D-printed jig. To ensure smooth and stable movement, a rail was installed between the linear actuator and the acrylic jig. The linear actuator was connected to

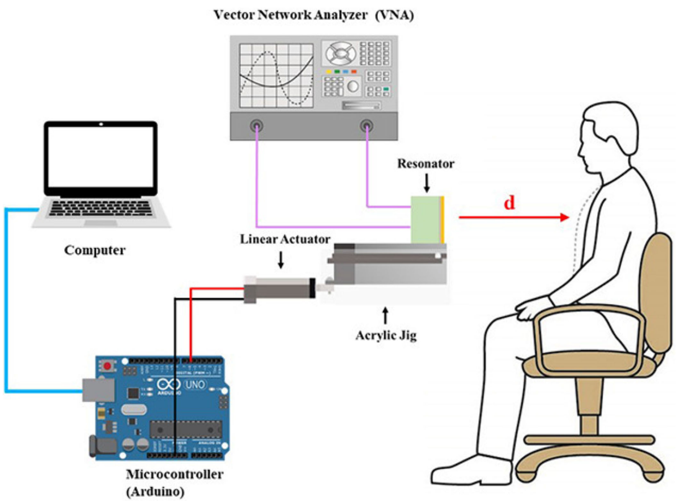

Fig. 9. Measurement setup for verifying the changes in the resonator characteristics.

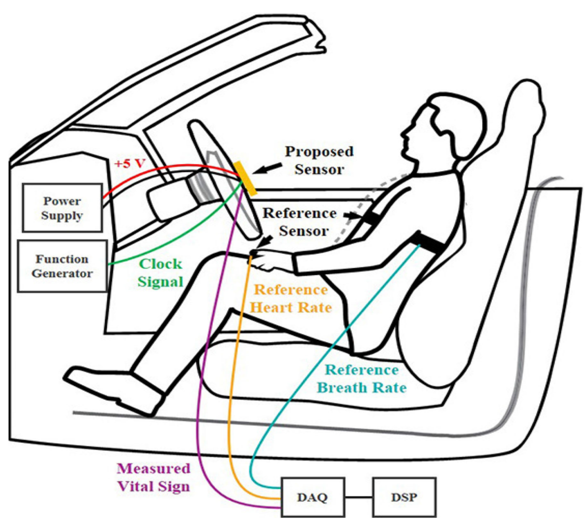

Fig. 10. Measurement setup in a real vehicle environment.

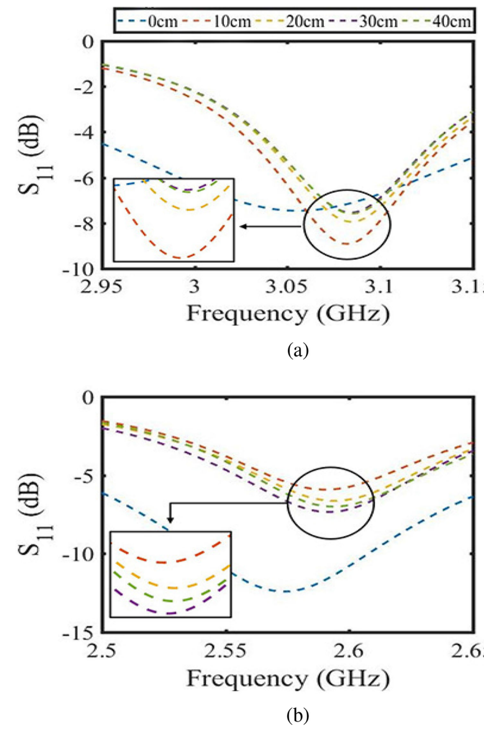

Fig. 11. Measurement results for frequency response vs. distance. (a) Resonator 1. (b) Resonator 2.

a microcontroller board, which was controlled by a computer, allowing the distance to be controlled from 0 cm to 40 cm in 1 cm increments.

A second set of experiments was conducted to verify the sensing response of the sensor when attached to a vehicle, as shown in Fig. 10. The performance of the proposed sensor was evaluated in comparison with commercial sensors. A physiological pulse transducer (UFI-1010) was fastened to the second finger of the driver to measure the heart rate, and a respiration transducer (UFI-1132) was fastened to the chest to measure the breath rate. The outputs of the proposed and reference sensors were sampled by a data acquisition (DAQ) board, which was controlled by LabView, and digital signal processing (DSP) was performed by the computer. The raw data from the proposed sensor were digitally bandpass filtered in the following two bands: 0.3–2 Hz to extract the respiration rate and 1–2 Hz to extract the heart rate. Because the signal strength from the lungs is much higher than that from the heart, the cutoff frequency band for the heart rate is narrower than that for the breath rate. The filtered results were visualized using the spectrogram method, which can show real-time beat rates via the short-time Fourier transform. This was done to ensure the reliability of the results by preventing the biased selection of results only from periods of good performance and by allowing transitions to be observed. Additionally, experiments were carried out with both male and female subjects to identify the effects of sex in a static vehicle.

III. Results and Discussion

A. Measuring the Variation in Impedance Versus Distance

As the distance (d) was varied from 0 cm to 40 cm, the frequency response of the each resonator was measured every 1 cm. For clear presentation of the experimental results, the frequency response of the resonators is presented for every 10 cm in Fig. 11(a) and Fig. 11(b). As the distance changes, the resonant frequency and radiation level of the resonator vary. Furthermore, to identify the null points, the first and second derivatives of the reactance of each resonator were derived, as shown in Fig. 12(a) and Fig. 12(b). The null points are clearly evident from the corresponding measurement errors, such as motion artifacts, difficulty in fixing the person at a specific location, and a lack of measurement points. As expected, the null points occur periodically with distance, and the intervals are similar to their analytical values. Resonator 1 has null points every 5 cm, starting at 6 cm, and resonator 2 has null points every 6 cm, starting at 7 cm; the half-wavelength of resonator 1 is 6.25 cm, and the half-wavelength of resonator 2 is 5.43 cm. Additionally,

TABLE II
AVERAGE VITAL SIGN SIGNALS IN A VEHICLE ENVIRONMENT (UNIT: BPM)

		Seatbelt		Corr.	Steering Wheel		Corr.
		Proposed	Reference		Proposed	Reference	
Male Subject	Breath Rate	25.42	25.57	0.92	22.47	22.77	0.98
	Heart Rate	59.00	59.09	0.90	54.80	55.69	0.92
Female Subject	Breath Rate	12.26	12.64	0.82	12.19	12.57	0.88
	Heart Rate	71.54	71.88	0.92	68.69	68.77	0.88

the variations in the derivatives of the reactance decrease with increasing distance, which can be explained in terms of the principles of electromagnetic radiation. Since the derivative values exhibit smaller changes, it is more difficult to detect the vital signs as the distance increases. However, the vital signs of a fellow passenger will not affect the results for the driver. By virtue of these characteristics, the proposed sensor can easily detect the vital signs of the driver through selective operation of the resonators via the switching circuit. Additionally, suitable results can be selected from the two resonators via postprocessing using DSP. If the results from one resonator are not consistent or are out of the expected ranges for the vital signs, then the results from the other resonator will be selected.

B. Operation of the Sensor When Installed in a Vehicle

To validate the reliability of the sensor, additional experiments were conducted in a static vehicle environment. First, the proposed sensor was attached to the seatbelt of the vehicle. Since the seatbelt is placed on the driver's body, both the lower and upper resonators can measure the vital signs of the human subject. Fig. 13(a)–(d) show the results measured with the proposed and reference sensors. All results from the proposed sensor are similar to those from the reference sensors, and the mean values of the strongest beat rates from each sensor are summarized in Table II. Moreover, the correlation coefficients between the proposed and reference sensors were calculated to validate the performance of the proposed sensor. To enhance the readability of the calculated results, unnecessary parts of the graphs have been removed, such as labels, ticks and scale bars. The correlation coefficient is calculated as follows:

$$Corr. = \frac{\sum_m \sum_n \left(A_{mn} - \overline{A}\right)\left(B_{mn} - \overline{B}\right)}{\sqrt{\left(\sum_m \sum_n \left(A_{mn} - \overline{A}\right)^2\right)\left(\sum_m \sum_n \left(B_{mn} - \overline{B}\right)^2\right)}}, \tag{5}$$

where corr. is the correlation coefficient; A and B are matrices generated from the results for the reference and proposed sensors, respectively, with m and n respectively denoting the rows and columns of each matrix; and $\overline{A}$ and $\overline{B}$ are the means of all values in A and B, respectively.

Due to the contact with the environment, unlike in the case of the reference sensors, undesired motion artifacts are also measured by the proposed sensor, as seen in Fig. 13(b) and 13(d). These motion artifacts cause the correlation coefficient to be low, as summarized in Table II. In addition, as is commonly known, females have faster heart rates than males do, and the observations are consistent with this fact.

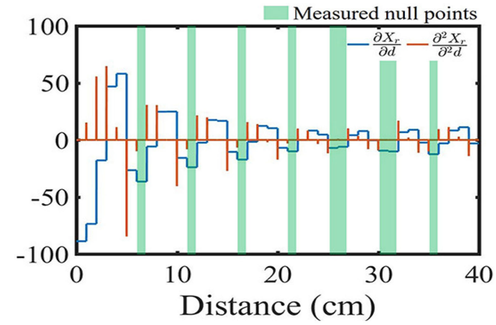

(a)

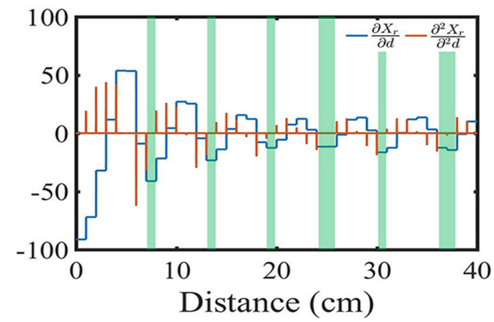

(b)

Fig. 12. Measurement results for impedance null points. (a) Resonator 1. (b) Resonator 2.

TABLE III
COMPARISON OF VITAL SIGN SENSOR PERFORMANCE

	Sensing Component	Detection Method	Detection Range	Size	Real-time Beat Rate
Lim [37]	Electrode	Static Capacitance	1.5 mm	16 cm^2	O
Ueno [38]	Electrode	Static Capacitance	1.0 mm	20 cm^2	O
Serra [39]	Antenna	Phase	Contact	115.06 cm^2	X
Kim [33]	Resonator	Impedance	20 mm	25 cm^2	X
Hong [34]	Resonator	Impedance	50 mm	30.25 cm^2	X
An [35]	Antenna	Impedance	50 mm	Not mentioned	X
Chang [40]	Resonator	Impedance	Contact	Not mentioned	X
This work	Resonator	Impedance	$\approx$ 400 mm	30.25 cm^2	O

Second, the proposed sensor was mounted on the steering wheel of the vehicle. The distance between the driver's body and the steering wheel was approximately 37 cm, vital signs extracted from resonator 1 were used. Since the distance between the sensor and the person was near the null point of resonator 2 and cause meaningless results. Fig. 14(a)–(d) compare the results from the proposed sensor and the reference sensors, and the results show excellent agreement, as summarized in Table II. In addition, our sensor also demonstrates superior performance compared to those reported in other works, as summarized in Table III.

IV. CONCLUSION

In this study, a novel vital sign sensor is proposed based on a switchable PLL-circuit-based architecture for the continuous noncontact monitoring of driver status. This sensor has been successfully demonstrated to detect vital signs when either attached to the seatbelt or mounted on the steering wheel

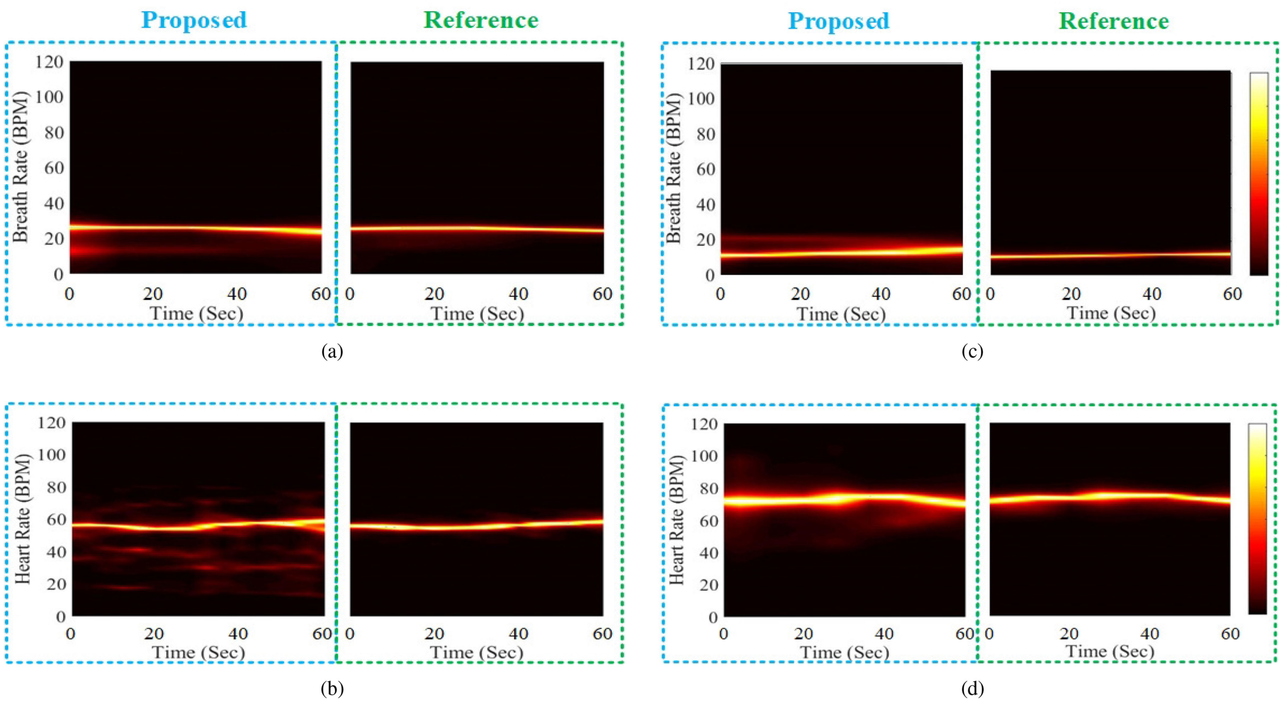

Fig. 13. Measurement results with the sensor attached to the seatbelt of a vehicle (0 cm), visualized as spectrograms. (a) Real-time breath rate of the male subject. (b) Real-time heart rate of the male subject. (c) Real-time breath rate of the female subject. (d) Real-time heart rate of the female subject.

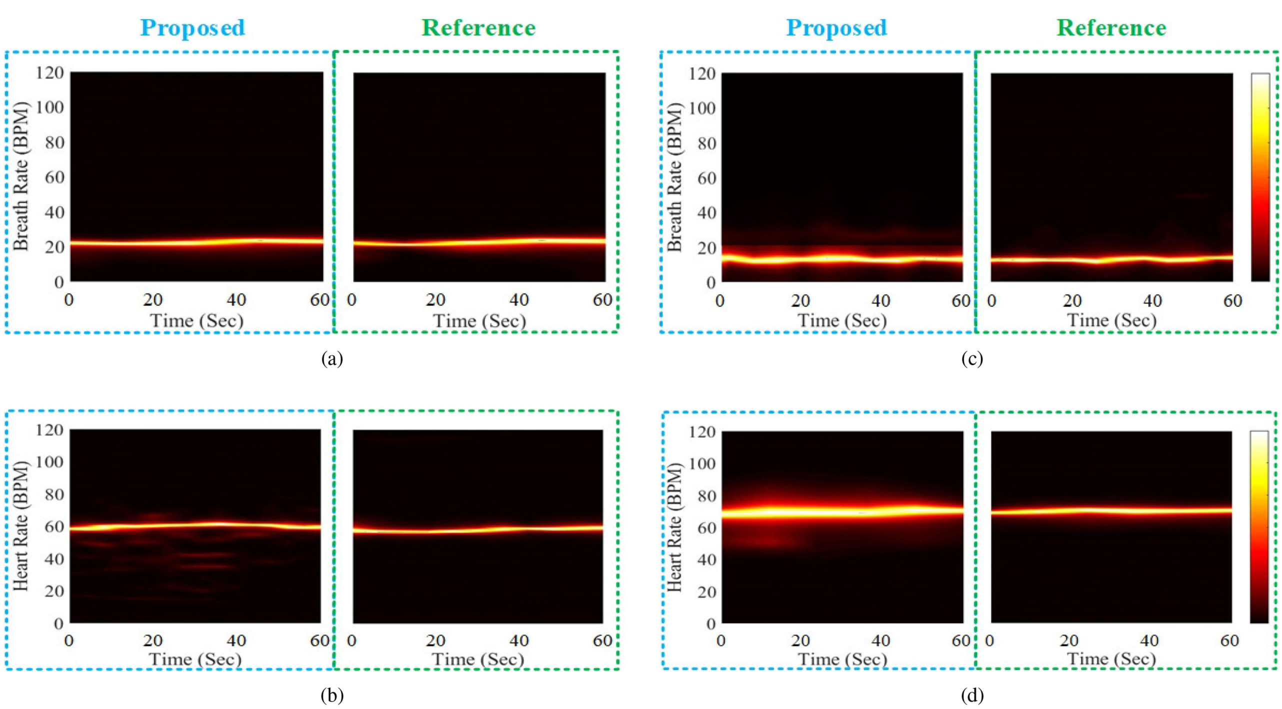

Fig. 14. Measurement results with the sensor mounted on the steering wheel of a vehicle (37 cm), visualized as spectrograms. (a) Real-time breath rate of the male subject. (b) Real-time heart rate of the male subject. (c) Real-time breath rate of the female subject. (d) Real-time heart rate of the female subject.

of a vehicle, regardless of the driver's sex. Additionally, the proposed sensor can detect both heart rate and breath rate simultaneously, without requiring separate sensors. The proposed sensor exhibits rapid response, excellent sensitivity, and good reproducibility. Furthermore, the detection range of the sensor is dramatically improved without increasing the size and complexity of the circuit. The proposed sensor clearly could be a excellent candidate for diagnosing driver status in real time in a vehicle environment. Future work will focus on reducing motion artifacts to enhance the stability and utility of the sensor in a moving vehicle. Moreover, the effects of temperature will be studied through cold and heat tests.

References

[1] A. Vaz *et al.*, "Full passive UHF tag with a temperature sensor suitable for human body temperature monitoring," *IEEE Trans. Circuits Syst. II. Express Briefs*, vol. 57, no. 2, pp. 95–99, Feb. 2010.

[2] S. Jetzki *et al.*, "A multisensor implant for continuous monitoring of intracranial pressure dynamics," *IEEE Trans. Biomed. Circuits Syst.*, vol. 6, no. 4, pp. 356–365, Aug. 2012.

[3] L. Peter, N. Noury, and M. Cerny, "A review of methods for non-invasive and continuous blood pressure monitoring: Pulse transit time method is promising?," *IRBM*, vol. 35, no. 5, pp. 271–282, 2014.

[4] J. Guo, "Uric acid monitoring with a smartphone as the electrochemical analyzer," *Analytical Chem.*, vol. 88, no. 24, pp. 11986–11989, 2016.

[5] J. Guo, and X. Ma, "Simultaneous monitoring of glucose and uric acid on a single test strip with dual channels," *Biosens. Bioelectron.*, vol. 94, pp. 415–419, 2017.

[6] J. Guo, "Smartphone-powered electrochemical biosensing dongle for emerging medical IoTs application," *IEEE Trans. Ind. Inf.*, vol. 14, no. 6, pp. 2592–2597, Jun. 2018.

[7] H. Choi *et al.*, "Design and in vitro interference test of microwave non-invasive blood glucose monitoring sensor," *IEEE Trans. Biomed. Circuits Syst.*, vol. 63, no. 10, pp. 3016–3025, Oct. 2015.

[8] C. Jang, J.-K. Park, H.-J. Lee, G.-H. Yun, and J.-G. Yook, "Temperature-corrected fluidic glucose sensor based on microwave resonator," *Sensors*, vol. 18, no. 11, 2018, Art. no. 3850.

[9] J. Guo, "Smartphone-powered electrochemical dongle for point-of-care monitoring of blood β-ketone," *Analytical Chem.*, vol. 89, no. 17, pp. 8609–8613, 2017.

[10] J. Guo, X. Huang, and X. Ma, "Clinical identification of diabetic ketosis/diabetic ketoacidosis acid by electrochemical dual channel test strip with medical smartphone," *Sens. Actuators. B. Chem.*, vol. 275, pp. 141–151, 2018.

[11] S. Lee *et al.*, "Real-time in vivo two-photon imaging study reveals decreased cerebro-vascular volume and increased blood-brain barrier permeability in chronically stressed mice," *Sci. Rep.*, vol. 8, 2018, Art. no. 13064.

[12] B. C. Tefft, "Prevalence of motor vehicle crashes involving drowsy drivers, united states, 1999–2008," *Accident Anal. Prevention*, vol. 45, pp. 180–186, 2012.

[13] X. Fan, B.-C. Yin, and Y.-F. Sun, "Yawning detection based on gabor wavelets and LDA," *J. Beijing Univ. Technol.*, vol. 35, pp. 409–413, 2009.

[14] P. M. Forsman, B. J. Vila, R. A. Short, C. G. Mott, and H. P. V. Dongen, "Efficient driver drowsiness detection at moderate levels of drowsiness," *Accident Anal. Prevention*, vol. 50, pp. 341–350, 2013.

[15] Z. Zhang and J. Zhang, "A new real-time eye tracking based on nonlinear unscented Kalman filter for monitoring driver fatigu," *J. Control Theory Appl.*, vol. 8, pp. 181–188, 2010.

[16] B. A. Shiferaw *et al.*, "Stationary gaze entropy predicts lane departure events in sleep-deprived drivers," *Sci. Rep.*, vol. 8, 2018, Art. no. 2220.

[17] A. Mittal, K. Kumar, S. Dhamija, and M. Kaur, "Head movement-based driver drowsiness detection: A review of state-of-art techniques," in *Proc. IEEE Int. Conf. Eng. Technol.*, 2016, pp. 903–908.

[18] J. Solaz *et al.*, "Drowsiness detection based on the analysis of breathing rate obtained from real-time image recognition," *Transp. Res. Procedia*, vol. 14, pp. 3867–3876, 2016.

[19] E. C.-P. Chua *et al.*, "Heart rate variability can be used to estimate sleepiness-related decrements in psychomotor vigilance during total sleep deprivation," *Sleep*, vol. 35, pp. 325–334, 2012.

[20] R. H. Brown, "The piezo solution for vital signs monitoring," *Med. Des. Technol.*, vol. 12, pp. 36–40, 2008.

[21] M. A. Ahmad, "Piezoelectric extraction of ecg signal," *Sci. Rep.*, vol. 6, 2016, Art. no. 37093.

[22] T. Tamura, Y. Maeda, M. Sekine, and M. Yoshida, "Wearable photoplethysmographic sensors-past and present," *Electronics*, vol. 3, no. 2, pp. 282–302, 2014.

[23] E. S. Winokur, T. O'Dwyer, and C. G. Sodini, "A low-power, dualwavelength photoplethysmogram (PPG) SOC with static and time-varying interferer remova," *IEEE Trans. Biomed. Circuits Syst.*, vol. 9, no. 4, pp. 581–589, Oct. 2014.

[24] Y. Kim and H. Ling, "Through-wall human tracking with multiple doppler sensors using an artificial neural network," *IEEE Trans. Antennas Propag.*, vol. 57, no. 7, pp. 2116–2122, Jul. 2009.

[25] O. Boric-Lubecke, V. M. Lubecke, A. Host-Madsen, D. Samardzija, and K. Cheung, "Doppler radar sensing of multiple subjects in single and multiple antenna systems," in *Proc. Int. Conf. Telecommun. ModernSatellite, Cable Broadcasting Services*, 2005, vol. 1, pp. 7–11.

[26] C. Li, V. M. Lubecke, O. Boric-Lubecke, and J. Lin, "A review on recent advances in doppler radar sensors for noncontact healthcare monitoring," *IEEE Trans. Microw. Theory Tech.*, vol. 61, no. 5, pp. 2046–2060, May 2013.

[27] A. Ahmad, J. C. Roh, D. Wang, and A. Dubey, "Vital signs monitoring of multiple people using a FMCW millimeter-wave sensor," in *Proc. IEEE Radar Conf.*, 2018, pp. 1450–1455.

[28] S. Kim and K.-K. Lee, "Low-complexity joint extrapolation-music-based 2-D parameter estimator for vital FMCW radar," *IEEE Sens. J.*, vol. 19, no. 6, pp. 2205–2216, Mar. 2019.

[29] S.-G. Kim, H.-J. Lee, J.-H. Lee, H.-I. Jung, and J.-G. Yook, "A highly sensitive and label free biosensing platform for wireless sensor node system," *Biosens. Bioelectron.*, vol. 50, pp. 362–367, 2013.

[30] Y. Hong, H.-J. Lee, S.-G. Kim, B.-H. Kim, G.-H. Yun, and J.-G. Yook, "A label-free biosensing platform using a PLL circuit and biotinstreptavidin binding system," *IEEE Trans. Biomed. Circuits Syst.*, vol. 9, no. 3, pp. 345–352, Jun. 2015.

[31] J.-K. Park, T.-G. Kang, B.-H. Kim, H.-J. Lee, H. H. Choi, and J.-G. Yook, "Real-time humidity sensor based on microwave resonator coupled with pedot: PSS conducting polymer film," *Sci. Rep.*, vol. 8, 2018, Art. no. 439.

[32] T.-G. Kang, J.-K. Park, G.-H. Yun, H. H. Choi, H.-J. Lee, and J.-G. Yook, "A real-time humidity sensor based on a microwave oscillator with conducting polymer pedot: PSS film," *Sens. Actuators. B. Chem.*, vol. 282, pp. 141–151, 2019.

[33] S.-G. Kim, G.-H. Yun, and J.-G. Yook, "Compact vital signal sensor using oscillation frequency deviation," *IEEE Trans. Microw. Theory Tech.*, vol. 60, no. 2, pp. 393–400, Feb. 2012.

[34] Y. Hong *et al.*, "Noncontact proximity vital sign sensor based on PLL for sensitivity enhancement," *IEEE Trans. Biomed. Circuits Syst.*, vol. 8, no. 4, pp. 584–593, Aug. 2014.

[35] Y.-J. An, G.-H. Yun, and J.-G. Yook, "Sensitivity enhanced vital sign detection based on antenna reflection coefficient variation," *IEEE Trans. Biomed. Circuits Syst.*, vol. 10, no. 2, pp. 319–327, Apr. 2016.

[36] X. Zhang and L. Zhu, "Gain-enhanced patch antennas with loading of shorting pins," *IEEE Trans. Antennas Propag.*, vol. 64, no. 8, pp. 3310–3318, Aug. 2016.

[37] Y. G. Lim, K. K. Kim, and K. S. Park, "ECG recording on a bed during sleep without direct skin-contact," *IEEE Trans. Biomed. Eng.*, vol. 54, no. 4, pp. 718–725, Apr. 2007.

[38] A. Ueno, Y. Akabane, T. Kato, H. Hoshino, S. Kataoka, and Y. Ishiyama, "Capacitive sensing of electrocardiographic potential through cloth from the dorsal surface of the body in a supine position: A preliminary study," *IEEE Trans. Biomed. Eng.*, vol. 54, no. 4, pp. 759–766, Apr. 2007.

[39] A. A. Serra, P. Nepa, G. Manara, G. Corsini, and J. L. Volakis, "A single on-body antenna as a sensor for cardiopulmonary monitoring," *IEEE Antennas Wireless Propag. Lett.*, vol. 9, pp. 930–933, 2010.

[40] T. Chang, C. Hsu, K. Chen, and C. Yang, "Wearable sensors based on a high sensitive complementary split-ring resonator for accurate cardiorespiratory sign measurements," in *Proc. Int. Microw. Symp.*, 2017, pp. 208–210.

Jin-Kwan Park (S'14) was born in Seoul, South Korea. He received the B.S. degree in electronics and electrical engineering from Dongguk University, Seoul, South Korea, in 2014. He is currently working toward the Ph.D. degree in electrical and electronics engineering with Yonsei University, Seoul, South Korea. His main research interests are RF based sensors such as vital-sign, humidity, glucose, and gas sensors, also microwave/millimeter-wave component/systems.

Yunseog Hong was born in Jeju, South Korea. He received the B.S. degree in telecommunication engineering from Jeju National University, Jeju, South Korea, in 1996, the M.S. degree in radio science and engineering from Kwangwoon University, Seoul, South Korea, in 2007, and the Ph.D. degree in electrical and electronics engineering from Yonsei University, Seoul, South Korea, in 2016. From January 1996 to August 2002, he joined KMW Inc., South Korea, as an Antenna System Engineer. From September 2002, he is currently working with Hanwha Systems, South Korea, as an Radar System Engineer. His main research interests are in microwave/millimeter wave components, active array radar system, remote wireless vital signal sensor, and RF bio-molecular sensor.

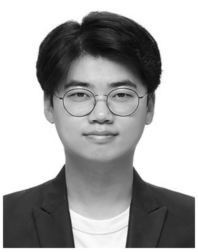

Hyunjae Lee (S'18) received the B.S. degree in electrical and electronics engineering from Yonsei University, Seoul, South Korea, in 2013, where he is currently working toward the Ph.D. degree in electrical and electronics engineering. His current research interests are in the remote vital sign sensors and radar signal processing.

Chorom Jang (S'18) was born in Incheon, South Korea. She received the B.S. degrees in electronic engineering from Seokyeong University, Seoul, South Korea, in 2017. She is currently working toward the Ph.D. degree in electrical and electronics engineering with Yonsei University, Seoul, South Korea. Her main research interests are RF based glucose sensor and microwave components.

Gi-Ho Yun was born in Jeonju-Si, South Korea. He received the M.S. and Ph.D. degrees in electronics engineering from Yonsei University, Seoul, South Korea, in 1986 and 1999, respectively. From 1985 to 1997, he was with Samsung Electronics and Samsung Electro-Mechanics. He was with Honam University, Gwangju, South Korea, from 1997 to 2008. He is currently an Associate Professor with the Division of Information and Communication Engineering, Sungkyul University, Anyang, South Korea. He is also with the Advanced Computational Electromagnetic Laboratory, Yonsei University, Seoul, South Korea. His current research interests include the areas of active and passive circuitry in the RF/MW frequency and various sensors detecting vital signals and bio signals in the human body.

Hee-Jo Lee received the Ph.D. degree in electrical and electronic engineering) from Yonsei University, Seoul, South Korea in 2012. From March 2010 to March 2012, he worked with Electrical and Electronic Engineering, Yonsei University and Graphene Research Institute, Sejong University, as a Postdoctoral Researcher, respectively. From April 2012 to August 2014, he also worked in Mechanical Engineering, Electrical and Electronic Engineering, Yonsei University, as a Research Professor. Since September 2014, he has been an Assistant Professor with the Department of Physics Education, Daegu University, Gyeongsan, South Korea. His main research interests are in the areas of electromagnetic wave and field theory, RF bio-and gas-sensors, RF circuit modeling and characterization of carbon nanomaterials, including graphene, graphene ribbon, graphene oxide, metamaterials, and plasmonics for biosensing.

Jong-Gwan Yook (S'89–M'97–SM'12) was born in Seoul, South Korea. He received the B.S. and M.S. degrees in electronics engineering from Yonsei University, Seoul, South Korea, and the Ph.D. degree from the University of Michigan, Ann Arbor, MI, USA, in 1987, 1989, and 1996, respectively. He is currently a Professor with the School of Electrical and Electronic Engineering, Yonsei University. His main research interests are in the areas of theoretical/numerical electromagnetic modeling and characterization of microwave/millimeter-wave circuits and components, design of radio frequency integrated circuits and monolithic microwave integrated-circuits, and analysis and optimization of high-frequency high-speed interconnects, including signal/power integrity (EMI/EMC), based on frequency as well as time-domain full-wave methods. His research team developed various biosensors, such as carbon-nano-tube RF biosensors for nanometer size antigen-antibody detection as well as remote wireless vital signal monitoring sensors.